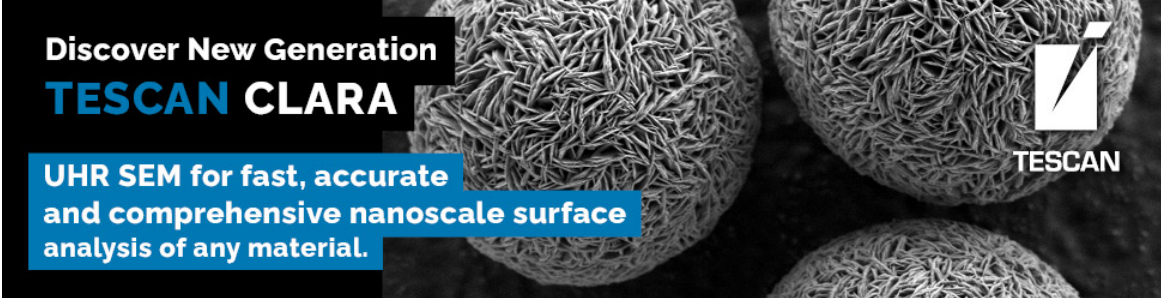



# Optical Measurement of the Stoichiometry of Thin-Film Compounds Synthetized From Multilayers: Example of Cu(In,Ga)Se<sub>2</sub>

Ricardo G Poeira, Daniel Siopa, Pedro Anacleto, Sascha Sadewasser, Phillip J Dale



Discover New Generation  
**TESCAN CLARA**

UHR SEM for fast, accurate  
and comprehensive nanoscale surface  
analysis of any material.



TESCAN

# Optical Measurement of the Stoichiometry of Thin-Film Compounds Synthesized From Multilayers: Example of Cu(In,Ga)Se<sub>2</sub>

Ricardo G. Poeira<sup>1,\*</sup> , Daniel Siopa<sup>1</sup>, Pedro Anacleto<sup>2</sup>, Sascha Sadewasser<sup>2</sup> , and Phillip J. Dale<sup>1</sup>

<sup>1</sup>Department of Physics and Materials Science, University of Luxembourg, 41, rue du Brill, L-4422 Belvaux, Luxembourg

<sup>2</sup>INL—International Iberian Nanotechnology Laboratory, Av. Mestre José Veiga s/n, 4715-330 Braga, Portugal

\*Corresponding author: Ricardo G. Poeira, E-mail: [ricardo.poeira@uni.lu](mailto:ricardo.poeira@uni.lu)

## Abstract

The properties of centimeter-sized thin-film compound semiconductors depend upon the morphology and chemical composition of the multiple submicrometer-thick elemental and alloy precursor layers from which they are synthesized. The challenge is to characterize the individual precursor layers over these length scales during a multistep synthesis without altering or contaminating them. Conventional electron and X-ray-based morphological and compositional techniques are invasive, require preparation, and are thus incompatible with in-line synthesis processes. In a proof-of-concept study, we applied confocal laser scanning microscopy (CLSM) as a noninvasive optical imaging technique, which measures three-dimensional surface profiles with nanoscale resolution, to this challenge. Using an array of microdots containing Cu(In,Ga)Se<sub>2</sub> semiconductor layers for solar cells as an example, we performed CLSM correlative studies to quantify morphological and layer thickness changes during four stages of a thin-film compound synthesis. Using simple assumptions, we measured the micrometer-scale spatially resolved chemical composition of stacked precursor layers to predict the final material phases formed and predict relative device performance. The high spatial resolution, coupled with the ability to measure sizeable areas without influencing the synthesis at high speed, makes CLSM an excellent prospect for research and quality control tool for thin films.

**Key words:** confocal laser scanning microscope, correlative spectroscopy, Cu(In,Ga)Se<sub>2</sub>, noninvasive *in situ* measurement, process monitor and control, sequential elemental stacks

## Introduction

Thin-film devices, such as thin-film solar cells (France et al., 2022), water splitting devices (Pan et al., 2020; Ye et al., 2021), thin-film batteries (Moitzheim et al., 2019; Yasuhara et al., 2019), or thin-film transistors (Choi et al., 2020; Shiah et al., 2021), contain multiple nanometer-to-micrometer-thick layers which require careful and precise morphological control during both research and industrial production phases. For the case of Cu(In,Ga)Se<sub>2</sub>-based thin-film solar cells, the most complicated layer within such a device stack is a multinary semiconductor layer, which itself is synthesized *in situ* on the device structure from the reaction of two or more so-called precursor layers and one or more reactive gasses. Despite this complexity, this approach is used in the world record power conversion efficiency of Cu(In,Ga)Se<sub>2</sub>-based solar cells (Nakamura et al., 2019). The layer thickness, morphology, and composition of the precursor layers critically influence the semiconducting properties of the final layers. Therefore, fast noninvasive in-line metrology of these precursor layers as well as the formed semiconductor after reactive annealing would enable a greater understanding of the synthesis process and also offer quality control.

Traditional thin-film metrology techniques are stylus profilometry, atomic force microscopy, scanning, or transmission electron microscopies, which can resolve surface features down to the nanoscale and allow to explore morphological

changes such as surface roughness, growth modes, particle size, shape, and distribution, as well as layer thickness. To perform local composition analysis, energy-dispersive X-ray spectroscopy (EDX) is suitable, and for large areas, X-ray fluorescence is commonly used given its accuracy. However, all of these techniques suffer from the risk of one or more of the following: alteration of the sample during measurement preparation, alteration of the sample by the characterization probe, vacuum exposure, or carbon deposited on the surface (Vladar & Postek, 2005). The drawbacks of these techniques imply that they are not suitable for investigating changes to the morphology or composition of a thin film as it flows through a multistep synthesis. Ideally, a method is needed that requires no alteration of the sample, uses a low-energy probe, measures large areas with micrometer precision on a time scale of minutes, allows analysis in an identical location after each process step, and leaves no contamination.

Confocal laser scanning microscopy (CLSM) is a rapid, noninvasive optical technique with tens of nanometer depth resolution, which enables the reconstruction of a three-dimensional (3D) representation of the material's surface. Two different modes have been developed: fluorescence and reflectance mode (Webb 1996). The reflectance mode relies on light reflection from the surface. The simplicity and flexibility of CLSM has motivated its application in a wide range of fields, in particular life science (Konishi et al., 2003; Jones et al., 2005; Blouin et al., 2018). In their review, Teng et al.

Received: March 31, 2023. Revised: July 26, 2023. Accepted: September 18, 2023

© The Author(s) 2023. Published by Oxford University Press on behalf of the Microscopy Society of America.

This is an Open Access article distributed under the terms of the Creative Commons Attribution License (<https://creativecommons.org/licenses/by/4.0/>), which permits unrestricted reuse, distribution, and reproduction in any medium, provided the original work is properly cited.

(2020) demonstrate the applicability of CLSM to material science with examples of characterization of surface structures (Yoon et al., 2006; Hongru et al., 2017; Merson et al., 2018), porous structures (Bruns et al., 2010; Yio et al., 2015), surface-modified groups (Li et al., 2018; Tian et al., 2019), spatial organization of microstructures (Lamprecht et al., 2000; Nishiyabu & Shimizu, 2016; Pyo et al., 2019), and also real-time analysis of crystal growth or chemical reactions (Wan et al., 2011; Cenker et al., 2012; Marcellini et al., 2016; Han et al., 2017). Phase formation, diffusion, or defect formation studies were also demonstrated with CLSM in diverse materials (Nakamura et al., 2009; Lin et al., 2012; Cao et al., 2021; Li et al., 2022a, 2022b), putting forward a wide range of applications. Given the success of CLSM in these applications, we hypothesized that it could be used in a multistep thin-film synthesis to not only follow morphology changes in identical locations but also perform compositional elemental analysis and correlative analysis.

In this study, we show how CLSM can be used in the in-line sequential synthesis of Cu(In,Ga)Se<sub>2</sub> (CIGSe) both locally on the hundreds of micron scale and globally over the wafer.

The sequential synthesis starts with the growth of the precursor metal layers (Cu, In, and Ga). In fact, to ensure the highest-quality CIGSe semiconductor layers, which help to produce high-efficiency devices, the precursor metal layers are required to be compact and smooth (Bi et al., 2016), and their relative elemental composition must be precisely controlled (Han et al., 2016). The crucial relative composition is monitored by the elemental ratio  $CGI = [Cu]/([Ga] + [In])$ , which is dictated by the thickness of the individual metal layers. To illustrate this concept, Figure 1 shows a schematic representation of a precursor stack and the resulting phases formed after the synthesis of the CIGSe semiconductor layer.

On the one hand, if the precursor stack contains more In and Ga atoms compared with Cu, a defective CIGSe phase, Cu<sub>1</sub>(In,Ga)<sub>3</sub>Se<sub>5</sub>, is expected to form (Zhang et al., 1998). On the other hand, in the case of a higher number of Cu atoms, the excess Cu atoms will form a detrimental secondary Cu<sub>2-x</sub>Se phase (Park et al., 2000). The exact CGI ratio controls the phases formed (Stanbery, 2002; Baek et al., 2011), carrier transport, optoelectronic properties, and the power conversion efficiency of the resulting solar cell (Siebentritt et al., 2013). Thus, we exploit the ability of CLSM to measure the thickness of thin films to monitor the precursor's CGI ratio.

Here, we present a proof of concept of using CLSM to obtain compositional information of thin films and show how

to use this information to anticipate material-phase formation after reactive annealing at the end of the synthesis. For this, we showcase a typical sequential synthesis process adapted to micro-solar cells for potential light concentration applications. With this work, we show the heretofore unrealized potential and general applicability of CLSM to thin-film synthesis in research and industry.

## Materials and Methods

CLSM is a noninvasive optical technique with micrometer spatial and nanometer depth resolution, which enables the reconstruction of 3D images of a specimen's morphology. In reflectance mode (Fig. 2), a laser light source is focused onto the sample's surface. The reflected light is filtered by a pinhole, which allows us to selectively detect the light that originated from the focal plane. A two-dimensional (2D) image of the surface features is obtained by rastering the laser using a set of scanning mirrors. Finally, a 3D image is obtained by assembling a stack of 2D images measured at the different focal plane positions. This process is also known as "optical sectioning".

CLSM measurements of an area yield both an optical image and a height map. Being able to measure the same region of interest before and after any process allows for the conduct of correlative studies and observation of the evolution of the sample to quantify the changes in morphology and even deduce elemental composition information. To demonstrate these concepts, we monitor a typical sequential synthesis process of micro-solar cells using CLSM and compare the morphological and compositional results with EDX and phase formation with micro-Raman spectroscopy.

The studied synthesis comprises the selective deposition and mixing of four elements to grow CIGSe semiconductor absorber layers in a templated array of microdots to form the lower half of the solar cells. Figure 3 shows a schematic of the four steps involved, starting from a 2 mm thick soda-lime glass substrate covered with a 500 nm thick molybdenum (Mo) layer onto which a 2 μm thick patterned SiO<sub>2</sub> mask was grown to allow for selective electrodeposition into an array of microdots (Sadewasser et al., 2017). Here, we define a dot to mean a hole in the SiO<sub>2</sub> with a diameter in the micrometer range reaching down to the underlying Mo. The first two synthesis steps are similar in that they consist of the electrodeposition of metal layers inside the 2 μm deep holes, where conductive Mo is exposed. In the first case, a Cu precursor layer is electrodeposited at 25°C, whereas in the second case, the

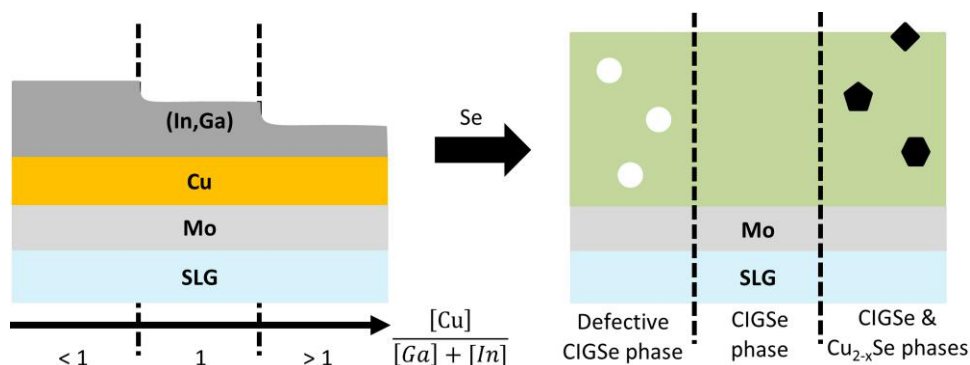


**Fig. 1.** Schematic representation of the metal precursor stack on molybdenum (Mo)-coated soda-lime glass (SLG), with three different CGI ratios and the respective resulting phases after reactive annealing in selenium to form the final CIGSe semiconductor layer. The relative thickness of the layers is not to scale.

co-electrodeposition of In and Ga is done simultaneously at 60°C (Siopa et al., 2020). At this stage, we obtain an array of stacked metals, which we denote as precursors. Subsequently, we perform a reactive annealing treatment of the precursor metal stacks in a Se-containing atmosphere (selenization) to incorporate the selenium, mix the elements uniformly, and finally form the micro-CIGSe semiconductor absorber layers (Poeira et al., 2023).

Before and after each step, we measured the images and height maps of all microdots with the CLSM. Since our process is sequential and we have a reference height plane that does not change ( $\text{SiO}_2$ ), we can track the evolution of the process. In Figure 4, we exemplify how to calculate an  $xy$ -resolved thickness map from the empty and electrodeposited Cu micro-layer height maps of one dot. First, we set the surrounding  $\text{SiO}_2$  matrix as the height reference (height = 0  $\mu\text{m}$ ) for all the involved height maps. Then, to obtain the Cu thickness map (Fig. 4c), we subtract the empty dot height map

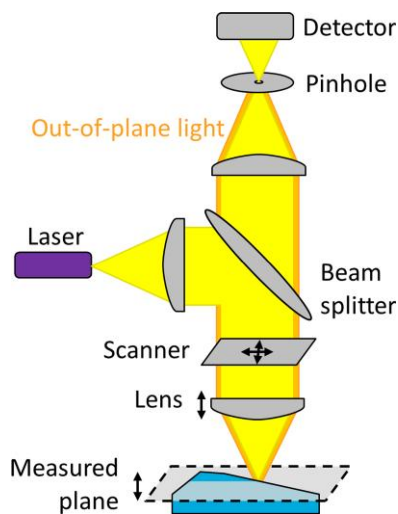


**Fig. 2.** Schematic representation of the confocal laser scanning microscopy components and working principle.

(Fig. 4a) from the Cu film height map (Fig. 4b). The attentive reader will notice that the empty dot depth, shown in Figure 4a, is calculated to be 0.5  $\mu\text{m}$  instead of the above-mentioned 2  $\mu\text{m}$ . This is due to the  $\text{SiO}_2$  being mostly transparent to the CLSM light source's wavelength, leading to an underestimated depth. However, since the  $\text{SiO}_2$  matrix is merely used as a reference plane, and is not modified throughout the process, the subtraction of the two height maps gives back a reliable thickness measurement, as elaborated in Supplementary material.

From the average thickness  $d$  of a layer, one can estimate the contained number of atoms  $N_x$ , that make up the layer, using equation (1) and assuming a constant volume density  $\rho_x$ , which we considered to be the bulk values. More precisely, we assume a density of 8.96  $\text{g/cm}^3$  for Cu, whereas for the In and Ga layers, we calculate a weighted average of the respective densities, 7.31  $\text{g/cm}^3$  for In and 5.90  $\text{g/cm}^3$  for Ga (Haynes et al., 2016). The surface area  $A$ , molar mass  $M_x$ , and Avogadro's number  $N_A$  are constants. Transforming the height data in this way allows us to perform elemental analysis.

$$N_x = \frac{\rho_x \cdot A \cdot N_A}{M_x} \cdot d \quad (1)$$

To complete the conversion of the micro-CIGSe semiconductors into solar cells, a 10 wt% potassium cyanide aqueous treatment is applied for 1 min to remove unwanted copper selenide phases, directly followed by a chemical-bath-deposited 50 nm CdS buffer layer (Sood et al., 2020). The window layers are composed of 50 nm intrinsic ZnO and 400 nm Al-doped ZnO, which were deposited by radio-frequency magnetron sputtering.

Optical images and height maps were acquired using a CLSM (Keyence VK-X1000) equipped with an UV laser (404 nm) and Nikon IC EPI PLAN lenses with magnification and respective numerical apertures of 5 $\times$ /0.13, 20 $\times$ /0.46, and 50 $\times$ /0.95 (APO). Except where specified otherwise, the height maps were measured using the 20 $\times$ /0.46 lens. The instrument's height measurement error is 12 nm for the

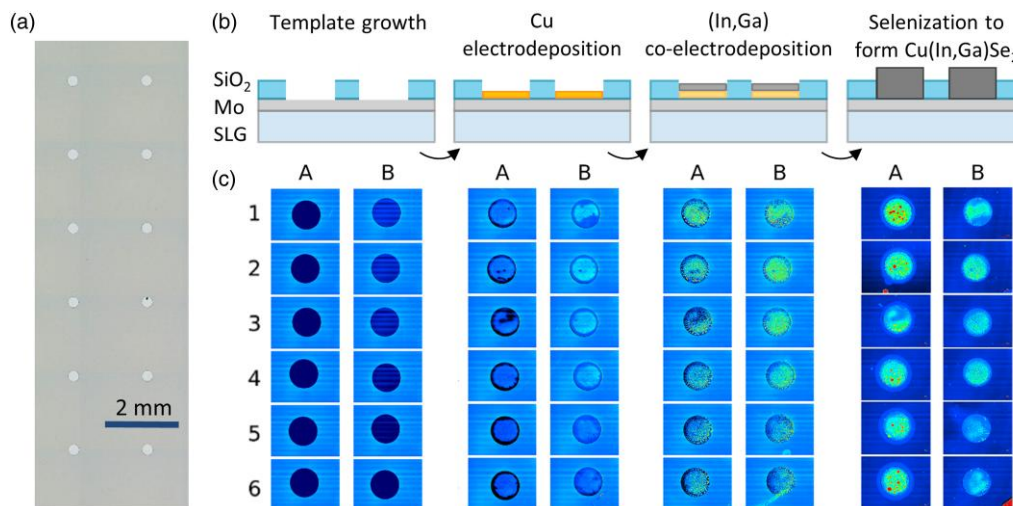


**Fig. 3.** (a) Optical image of a fraction of the array with empty dots, measured with a 5 $\times$ /0.13 lens. The exposed Mo layer has a silverish appearance. (b) Schematics of the micro-CIGSe semiconductors multistep synthesis process. Schematics are not to scale:  $\text{SiO}_2$  thickness  $\sim 2 \mu\text{m}$ , dot diameter 300  $\mu\text{m}$ , center-to-center distance 2 mm. (c) Confocal laser scanning microscopy measured the height maps of the dots at the different stages of the synthesis.

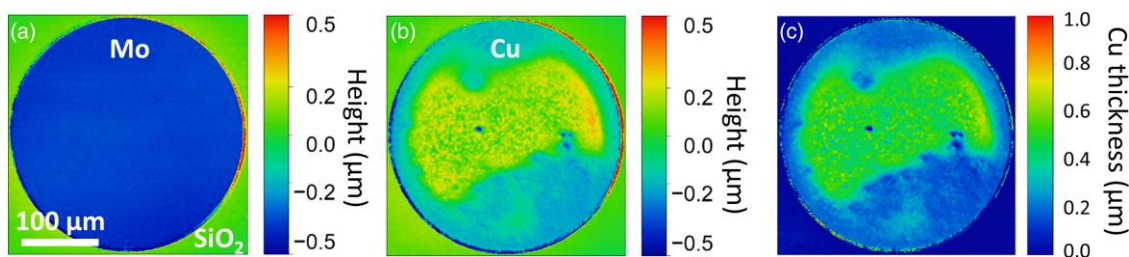


**Fig. 4.** Confocal laser scanning microscopy height maps for (a) empty dot and (b) electrodeposited Cu film. (c) Electrodeposited Cu film thickness calculated from height maps:  $c = b - a$ . The region surrounding the microdot is an insulating  $\text{SiO}_2$  matrix that was set to a zero-reference height. Note the change in intensity scale for (c).

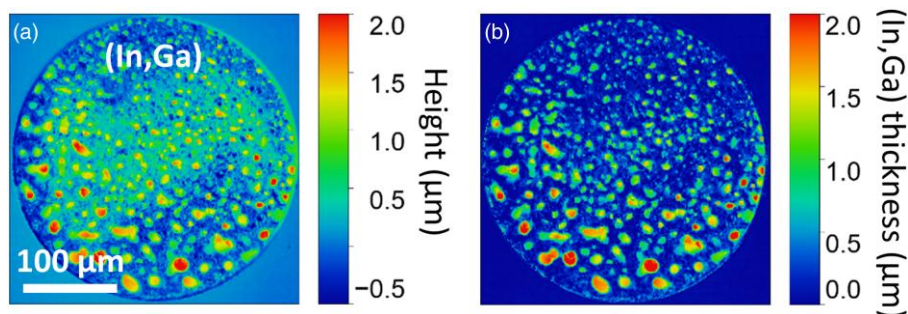


**Fig. 5.** (a) Confocal laser scanning microscopy height map for Cu(In,Ga) stack. (b) Calculated (In,Ga) film thickness from stack's height and Cu thickness maps. Note each image has a different scale.

50×/0.95 lens and 40 nm for the 20×/0.46 lens. The time for the acquisition of one image, and respective height map, is about 30 s for the system mentioned. In addition, elemental mappings were recorded with a Zeiss EVO10 microscope coupled with an UltimMax40 detector for EDX. Material-phase analysis was performed using a Renishaw inVia micro-Raman spectrometer equipped with a 532 nm laser excitation in conjunction with a 2,400 lines/mm grating. After device completion, each microsolar cell was electrically isolated by tape masking before sputtering the window layers. Current–voltage (JV) curves were measured under AM1.5 illumination using an AAA-class solar simulator.

## Results and Discussion

As discussed in the introduction, to ensure the highest-quality CIGSe layers, which lead to high-efficiency devices from stacked precursor layers (Bi et al., 2016; Siopa et al., 2020), we aim to produce compact, smooth, and thickness-controlled metal layers. An example of the contrary case is shown in Figure 4, where a nonuniform thickness distribution is observed, with a preferential growth of Cu at the center of the dot, leading to a thinner Cu layer at the periphery. This could be explained by an inhomogeneously oxidized or contaminated Mo surface in this particular microdot, which influences the nucleation process during the early stages of the electrodeposition (Bi et al., 2016; Hamdi et al., 2021).

Moving on to the co-electrodeposition of In and Ga, one can isolate the thickness map of the In,Ga layer (Fig. 5b) from the Cu(In,Ga) microprecursor stack height map (Fig. 5a) by proceeding similarly as detailed previously for the Cu layer.

The typical formation of In islands embedded in a In,Ga alloy layer is observed, as reported in the literature (Malaquias et al., 2014). Merely from the height map (i.e., top view) of the

Cu(In,Ga) stack, we cannot distinguish whether the deposition of In and Ga was homogeneous, as the underlying inhomogeneous Cu layer highly affects its morphology. However, by isolating the thickness map of the In,Ga layer from the metal stack (see Fig. 5b), it is visible that the In islands grew preferentially at the lower edge of the microdot.

The analysis is extended to the complete array of 49 microdots, allowing us to perform statistics and analyze wafer-scale effects. Figure 6 shows maps of the average layer thickness and respective root mean square (RMS) roughness on each individual microdot that makes up the array.

By associating each thickness value with the respective array position, we can study the spatial distribution of the microdots' thicknesses, as shown in Figures 6a and 6b. With this representation, we observe that in general, the average thickness of Cu deposited in each dot was similar, with a few outliers, suggesting that some microdots had a contaminated Mo surface prior to the deposition, which may have caused a locally unfavorable growth. However, looking at the In and Ga spatial distribution, a thickness gradient is clearly present from the periphery to the center of the array. Uniformly thick In and Ga deposits can be achieved over larger areas than those mentioned here if a sufficiently negative potential is applied above a threshold to the substrate (Malaquias et al., 2014). If the potential is below this threshold, the rate of electrodeposition will proceed slower in the middle. Electrical contacts to the array are made on the corners of the wafer, and we propose here that either the deposition potential was insufficiently negative or the Mo resistance was higher than expected, both leading to a more positive potential toward the array center and thus less In and Ga deposition. With regard to the distribution of layer' thickness, we note that the target was to electrodeposit 330 nm of Cu and 550 nm of In and Ga per microdot. From the thickness distribution in Figure 6c, we

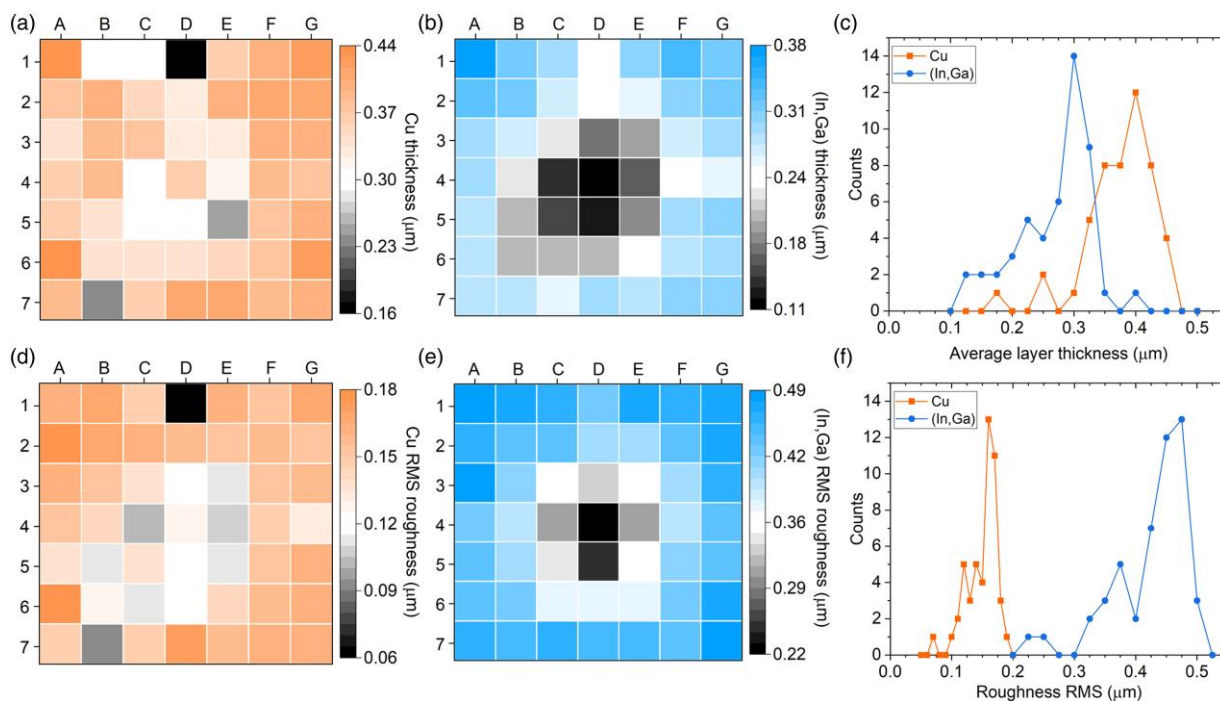


**Fig. 6.** Array statistics of Cu and (In,Ga) layers average thickness (a–c) and roughness (d–f). Heatmap representation of the array of Cu layers' (a) thickness and (d) RMS roughness. Heatmap of (In,Ga) layers' (b) thickness and (e) RMS roughness. Frequency distribution of the 49 microdots of Cu and In,Ga (c) layer thickness and (f) RMS roughness. Thickness measurement error is  $\pm 0.08 \mu\text{m}$ .

**Table 1.** Average CGI Ratio of a MicroPrecursor Array Measured with (a) CLSM and (b) EDX. A color scale was applied to both tables, where blue indicates a low CGI ratio and red refers to a high CGI within the respective dataset.

(a)	A	B	C	D	E	F	G
1	2.4	1.9	2.1	1.4	2.4	2.4	2.8
2	2.4	2.6	2.8	2.9	3.2	2.8	2.7
3	2.5	2.9	3.5	4.0	3.6	3.1	2.9
4	2.6	3.7	4.6	6.9	4.1	3.4	3.0
5	2.7	3.6	4.5	5.0	2.8	2.7	2.8
6	3.2	3.4	3.5	3.5	3.1	2.8	3.0
7	2.8	1.8	2.8	2.9	3.0	2.6	2.7

(b)	A	B	C	D	E	F	G
1	0.9	0.9	0.9	0.6	1.0	0.9	0.9
2	1.0	1.0	1.0	1.2	1.0	0.9	0.9
3	0.8	1.1	1.3	1.4	1.2	1.0	0.9
4	1.1	1.3	1.0	2.0	1.4	1.1	1.0
5	1.1	1.3	1.5	1.8	1.3	1.1	0.9
6	1.0	1.3	1.2	1.4	1.3	1.0	0.9
7	1.1	0.8	1.1	1.0	1.0	1.3	0.9

calculated an average thickness of 360 nm with a deviation of 50 nm, which is in agreement with the expected value. However, in the case of In and Ga, we found an average thickness of  $260 \pm 60$  nm, which deviates from the expected thickness. We believe that this is attributed to the low faradaic efficiency of the co-electrodeposition.

Proceeding with the roughness spatial distribution of Cu and In and Ga layers, in Figures 6d and 6e, one notices a close correlation with the respective thickness maps, as in general, the roughness increases along with the layer's thickness. Indeed, the microdots at the center were relatively thin, leading to low roughness, whereas the peripheral microdots grew thicker, with taller In islands, causing high roughness. As for the layers' roughness distribution (Fig. 6f), we observe that the Cu layers are considerably smoother compared with the (In,Ga) layers, which is inherently linked to the island growth mode of In during the co-electrodeposition (Malaquias et al., 2014). Additionally, the roughness distribution of (In,Ga) is much broader than that of Cu due to the potential edge-to-center gradient mentioned previously.

The morphology study allowed us to investigate the growth process and provided statistics on the metallic layers, both at microdot and array levels. As explained in the methods, we can relate the thickness of each layer with the number of constituent atoms, which opens the possibility of estimating the stacks' composition with CLSM. Therefore, from the thickness maps of the two layers, one can calculate both an average and a spatially resolved map of the characteristic composition ratio  $\text{CGI} = [\text{Cu}]/([\text{Ga}] + [\text{In}])$ . As discussed in the introduction, controlling the CGI ratio is critical to achieve high-quality CIGSe semiconductor material, thus monitoring this parameter without influencing or contaminating the synthesis process is important. To simplify our composition calculation, we assume no interdiffusion occurred between the two deposited layers. In Table 1a, we summarize the average CGI ratio of each microprecursor in the array, which was calculated using the respective CLSM thickness maps. To cross-check the validity of the calculation, an average composition of each microprecursor was also measured with large-area EDX and shown in Table 1b.

To facilitate comparison, we applied a common color scale to both tables to illustrate the positive correlation (correlation coefficient: 0.85) between the two data sets. It is worth noting that EDX compositional analysis on layered stacks is not straightforward (Fitting et al., 1997, 2007), which explains the need for a conversion factor to relate the two data sets. Despite this, the high correlation means that CLSM can, in principle, reliably measure the microprecursor's CGI ratio.

Above, we compared the CGI ratio of the microprecursors to prove the concept; however, ultimately, the parameter of interest is the final semiconductors' CGI ratio, where the precursor bi-layer structure is reacted away and all the elements have intimately mixed to form the CIGSe compound. For this, we use a set of microprecursors which span the CGI interval of interest for device fabrication. Thus, we compare the CGI ratio of the microprecursors from CLSM with CGI measured from EDX after selenization, meaning, after the formation of the CIGSe semiconductor, as plotted in Figure 7. To maximize vertical resolution, the measurements are performed by using the 50×/0.95 lens. The results show a direct linear trend between CLSM precursor CGI ratio and EDX semiconductor CGI ratio, implying that the average composition of the final CIGSe semiconductor can be measured accurately with CLSM before

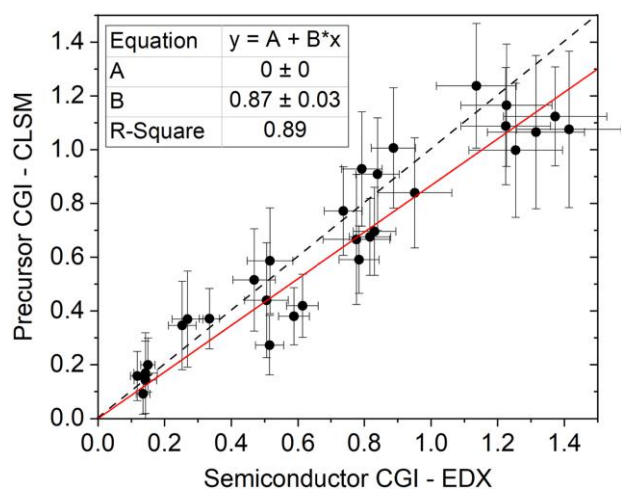


**Fig. 7.** Compositional CGI ratio of precursor stack measured with confocal laser scanning microscopy compared with the final CIGSe semiconductor layer CGI ratio measured with energy-dispersive X-ray spectroscopy. Linear fitting parameters are shown as inset. Solid line is a linear fit, whereas dashed line corresponds to the ideal case  $y=x$ . A 50×/0.95 lens was used for this set of measurements.

the reactive annealing step. Assuming that EDX perfectly describes the CGI ratio, we hypothesize that our fit deviates from the ideal case ( $y=x$ ), due to the peculiar morphology of the In and Ga alloy layer which changes spatially.

Going one step further and exploiting the micrometer spatial resolution of the CLSM thickness maps, one can compute a qualitative CGI ratio map for each dot by calculating the ratio between the Cu and In and Ga thickness maps, as shown in Figure 8a. Given the z-resolution of CLSM, some pixels in the In and Ga thickness map displayed a value close to zero or even negative, which would distort the CuGaIn scale bar. To prevent this distortion, we have zeroed any negative value and added 10 nm, which is below the CLSM resolution, to the In and Ga layer thickness map before calculating the CuGaIn map. Looking inside a single microdot helps to distinguish between high CuGaIn (Cu-richer) and low CGI ratio (Cu-poorer) regions, which has been shown to be critical for the formation of secondary phases, impacting the performance of the CIGSe semiconductor (Grabitz et al., 2006; Abou-Ras et al., 2018).

For a direct comparison, an EDX elemental map was measured before and after selenization, and CuGaIn maps of the precursor and semiconductor were calculated in Figures 8b and 8c, respectively. Focusing on the precursor CuGaIn maps, one can observe that both techniques yield a similar CGI distribution within the microdot. The calculated precursor CGI ratio maps are characterized by dark blue patches arising from the morphology of the In islands that typically form during the co-electrodeposition step (Malaquias et al., 2014). Indeed, a larger concentration of In results in a low CGI ratio. Conversely, the central region of the microdot shows a high CGI ratio, which comes about due to the observed preferential deposition of Cu in this area for this particular microdot. Consequently, after selenization, we expect a higher CGI ratio in this central region compared with the periphery. The resulting CGI spatial distribution of the semiconductor, shown in Figure 8c, corroborates with the conclusions drawn from the CLSM precursor CGI map in the sense that the central region of the semiconductor shows indeed a high CGI ratio, whereas a low CGI characterizes the periphery. Nevertheless, the effect of the diffusion of elements during the selenization process is clearly visible when comparing both CGI maps. In fact, the precursor's In islands are completely smeared out after the CIGSe formation, whereas the Cu-rich central region is still identifiable, which suggests that the lateral diffusion length of Cu is not high enough to homogenize the CGI distribution from the precursor. Thus, in our sequential process, the morphology

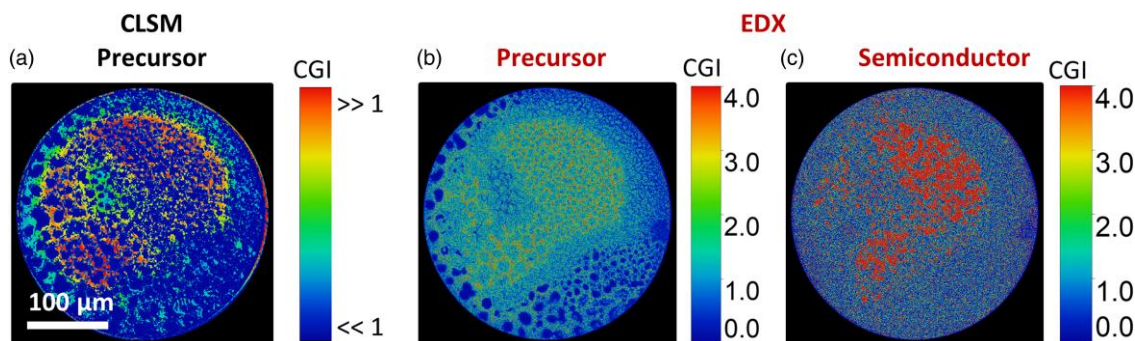


**Fig. 8.** Spatially resolved CGI mapping of: (a) precursor stack measured with confocal laser scanning microscopy with noncalibrated scaling due to the divide by zero error discussed in the text, (b) precursor stack measured with energy-dispersive X-ray spectroscopy (EDX), and (c) semiconductor stack measured with EDX.

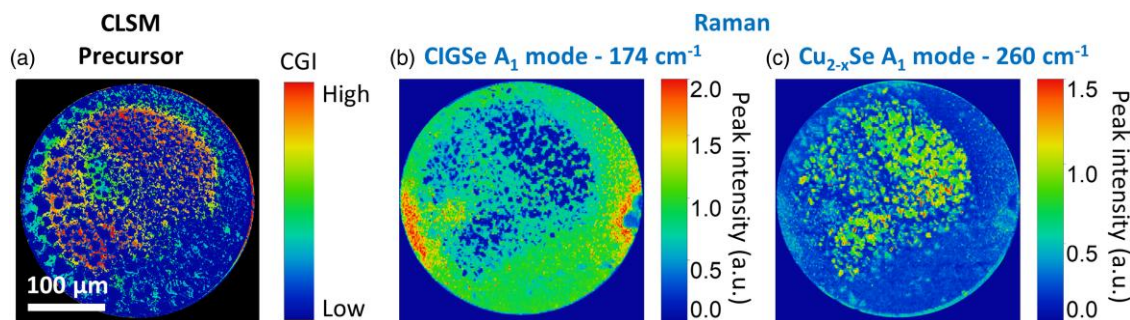


**Fig. 9.** (a) Spatially resolved CGI ratio mapping of precursor stack measured with confocal laser scanning microscopy. Raman intensity mapping of final semiconductor: (b) CIGSe  $A_1$  mode at  $174\text{ cm}^{-1}$  and (c)  $\text{Cu}_{2-x}\text{Se}$   $A_1$  mode at  $260\text{ cm}^{-1}$ .

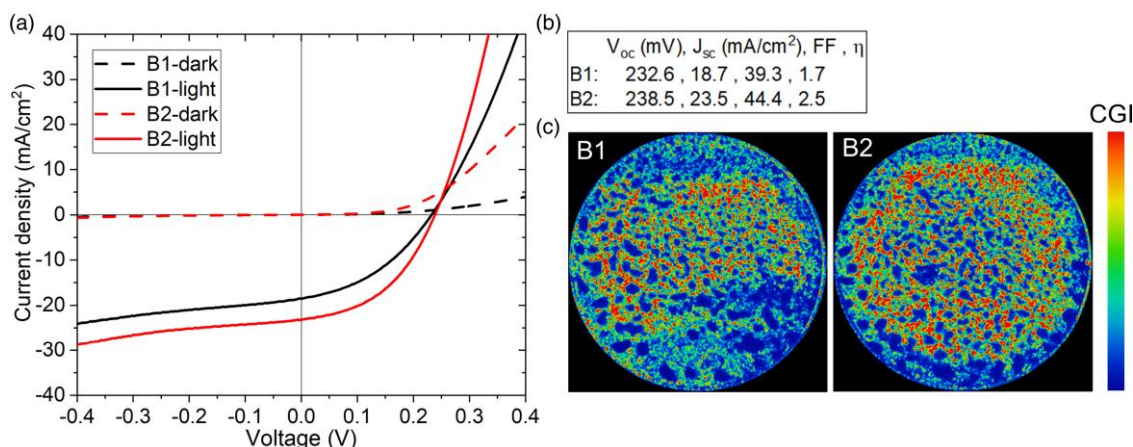


**Fig. 10.** (a) Measured JV characteristics of two microsolar cells based on semiconductors B1 and B2. (b) Table summarizing main JV parameters of both devices. (c) B1 and B2 precursor CGI distribution maps are shown. To reduce noise on maps, a two-pixel Gaussian smoothing was applied to both CGI distributions.

of the Cu layer must be smooth and uniformly thick to achieve a homogeneous CGI distribution.

With the CLSM information, one can anticipate the semiconductor's CGI lateral profile from the precursor. Furthermore, knowing the composition's spatial distribution beforehand allows us to anticipate which phases are more likely to form in the different regions of interest, by referring to the material's phase diagram. In our case, assuming a sufficient supply of Se during selenization, a CGI > 1.0 results in the formation of a conductive secondary phase, namely  $\text{Cu}_{2-x}\text{Se}$ , in addition to the main CIGSe phase of interest. Referring back to our CGI profiles, in Figure 8, the regions more likely to form a  $\text{Cu}_{2-x}\text{Se}$  phase are the regions shown in red. To confirm this hypothesis, we measure micron-resolved Raman spectroscopy which provides information on the vibrational modes of the crystalline structures and allows us to identify the phases that are present at the surface of the material. Reports in the literature show the main vibrational modes of CIGSe and  $\text{Cu}_{2-x}\text{Se}$  in Raman are characterized by intense peaks at  $174$  and  $260\text{ cm}^{-1}$ , respectively (Witte et al., 2006, 2008; Schmid et al., 2016). To have spatial information, a map of spectra was acquired, from the same semiconductor discussed in Figure 8 (repeated in Fig. 9a for easier comparison), and the intensities measured at  $174$  and  $260\text{ cm}^{-1}$  are mapped in Figures 9b and 9c, respectively. As a guideline, a higher intensity suggests the respective phase is present and lower intensity means it is absent.

First, it is worth noting that the Raman maps have the same pattern as observed in the previously discussed CGI ratio

maps. In fact, we observe that the high CGI region matches the spatial distribution of the  $\text{Cu}_{2-x}\text{Se}$  phase from Raman, which corroborates with the material's phase diagram. Regarding the CIGSe phase, one can see that it is the main phase present in the lower CGI region in the CGI maps. Note that since Raman is surface sensitive, one cannot draw information from the phases present in the bulk, which is also why the Raman maps are complementary.

Finally, two micro-CIGSe semiconductors (B1 and B2), with different CGI spatial distributions, were completed into devices and the current–voltage (JV) curve was measured (see Fig. 10a). The CGI distribution of the latter semiconductor was more homogeneous throughout the dot compared with that of the former semiconductor (see Fig. 10c). As shown in Figure 10, the most homogeneous semiconductor shows a higher power conversion efficiency; however, we suspect that its absolute value is still relatively low due to the Cu-rich (CGI > 1.0) nature of the overall precursor, which is known to strongly deteriorate performance.

## Conclusions

This work shows that CLSM enables a noninvasive investigation of multistep thin-film synthesis processes. We have showcased our CIGSe microsolar cell synthesis process, where we have performed statistical analysis at individual microdot and array levels. We demonstrate how to measure precursor composition in sequential processes and how it



correlates to the formation of different material phases after an annealing process. The two major findings of this work are that with simple assumptions, we can calculate the elemental ratio of the semiconductor and that monitoring the individual components allows us to do correlative spectroscopy studies and study how the system evolves from one step to the following. Thus, we can predict the composition and anticipate inhomogeneities within the precursor resulting in a less-performing device. In the future, we will investigate new electrodeposition bath chemistries and plating routines for Cu, In, and Ga deposition into the arrays of holes, and we will be able to investigate and compare height inhomogeneities and roughness values between the different process conditions in a statistically significant manner, given the large number of dots on each array. By examining the distribution of the elements, we will be able to anticipate in advance and make correlations with the quality of our semiconductor devices.

The CLSM analysis approach presented in this work is easily transferred to other multistep synthesis such as thin-film batteries and transistors, microstructured layers, etc. Furthermore, despite the demonstrated synthesis being additive, the CLSM analysis is equally compatible with subtractive processes such as photolithography. Two caveats for the general use of this method are that (i) the layers' surface of interest should be sufficiently reflective to avoid erroneous measurements caused by reflections from underlying interfaces and (ii) the absolute values of the elemental ratios depend on knowing the density of the deposited layers. The additional advantages of CLSM are that it involves no sample preparation, and measurements of arrays or large areas are possible within a timescale of minutes. These combined advantages show that CLSM can be applied to both industrial quality control and research for conducting fundamental analysis such as diffusion studies in thin films.

## Supplementary Material

To view [supplementary material](http://academic.oup.com/mam/article-lookup/doi/10.1093/mam/ozad105#supplementary-data) for this article, please visit <http://academic.oup.com/mam/article-lookup/doi/10.1093/mam/ozad105#supplementary-data>.

## Acknowledgments

For the purpose of open access, the author has applied a Creative Commons Attribution 4.0 International (CC BY 4.0) license to any author-accepted manuscript version arising from this submission.

## Financial Support

This research was partly funded by the Luxembourg National Research Fund (FNR), grant reference (PRIDE17/12246511/PACE). The authors acknowledge the additional support provided by the “Microconcentrator thin film solar cells (MiconCell)” project (PTDC/CTM-CTM/28922/2017) co-funded by FCT and ERDF through COMPETE2020.

## Conflict of Interest

The authors declare that they have no competing interest.

## References

Abou-Ras D, Schäfer N, Hages CJ, Levchenko S, Márquez J & Unold T (2018). Inhomogeneities in Cu(In, Ga)Se<sub>2</sub> thin films for solar cells: Band-gap versus potential fluctuations. *Solar RRL* 2(1), 1700199. <https://doi.org/10.1002/solr.201700199>

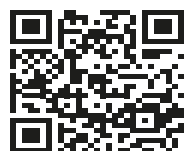
- Baek ER, Astini V, Tirta A & Kim B (2011). Phase evolution of CIGS alloyed compound synthesis by direct melting method. *Curr Appl Phys* 11(1), S76–S80. <https://doi.org/10.1016/j.cap.2010.11.091>
- Bi J, Yao L, Ao J, Gao S, Sun G, He Q, Zhou Z, Sun Y & Zhang Y (2016). Pulse electro-deposition of copper on molybdenum for Cu(In, Ga)Se<sub>2</sub> and Cu<sub>2</sub>ZnSnSe<sub>4</sub> solar cell applications. *J Power Sources* 326, 211–219. <https://doi.org/10.1016/j.jpowsour.2016.07.005>
- Blouin S, Roschger A, Varga F, Misof B, Spitzer S, Roschger P & Klaushofer K (2018). Confocal laser scanning microscopy—a powerful tool in bone research. *Wien Med Wochenschr* 168(11–12), 314–321. <https://doi.org/10.1007/s10354-018-0639-x>
- Bruns S, Müllner T, Kollmann M, Schachtner J, Hötzel A & Tallarek U (2010). Confocal laser scanning microscopy method for quantitative characterization of silica monolith morphology. *Anal Chem* 82(15), 6569–6575. <https://doi.org/10.1021/ac100909t>
- Cao J, Zeng Z, Zhang F, Guo D & Hou Z (2021). Effect of cooling rates on the local—overall morphology characteristics of solidification structure at different stages for high carbon steel. *Metals (Basel)* 11(8), 1291. <https://doi.org/10.3390/met11081291>
- Çenker ÇÇ, Bomans PHH, Friedrich H, Dedeoğlu B, Aviyente V, Olsson U, Sommerdijk NAJM & Bucak S (2012). Peptide nanotube formation: A crystal growth process. *Soft Matter* 8(28), 7463. <https://doi.org/10.1039/c2sm25671a>
- Choi S, Kang C, Byun C-W, Cho H, Kwon B-H, Han J-H, Yang J-H, Shin J-W, Hwang C-S, Cho NS, Lee KM, Kim H-O, Kim E, Yoo S & Lee H (2020). Thin-film transistor-driven vertically stacked full-color organic light-emitting diodes for high-resolution active-matrix displays. *Nat Commun* 11(1), 2732. <https://doi.org/10.1038/s41467-020-16551-8>
- Fitting H-J, Cornet N, Salh R, Guerret-Piécourt C, Goerriot D & von Czarnowski A (2007). Electron beam excitation in thin layered samples. *J Electron Spectrosc Relat Phenom* 159(1–3), 46–52. <https://doi.org/10.1016/j.elspec.2007.03.014>
- Fitting HJ, Kuhr JC, Goldberg M, Becher B & Barfels T (1997). EDX depths analysis of MIS-structures. *Mikrochim Acta* 125(1–4), 235–238. <https://doi.org/10.1007/BF01246189>
- France RM, Geisz JF, Song T, Olavarria W, Young M, Kibbler A & Steiner MA (2022). Triple-junction solar cells with 39.5% terrestrial and 34.2% space efficiency enabled by thick quantum well superlattices. *Joule* 6(5), 1121–1135. <https://doi.org/10.1016/j.joule.2022.04.024>
- Grabitz PO, Rau U, Wille B, Bilger G & Werner JH (2006). Spatial inhomogeneities in Cu(In, Ga)Se<sub>2</sub> solar cells analyzed by an electron beam induced voltage technique. *J Appl Phys* 100(12), 124501. <https://doi.org/10.1063/1.2402345>
- Hamdi R, Rached A, Massoudi I, Al-Zuraie R, Al-Hamad K, Al-Otaibi A, Flemban T, Alonizan N & Ghrib T (2021). Electrodeposition study of silver: Nucleation process and theoretical analysis. *J Electron Mater* 50(10), 5507–5513. <https://doi.org/10.1007/s11664-021-09055-8>
- Han A, Huang Y, Liu X, Xian W, Meng F & Liu Z (2016). Morphology, structure, and properties of Cu-poor and Cu-rich Cu(In, Ga)Se<sub>2</sub> films partially selenized using H<sub>2</sub>Se gas. *Jpn J Appl Phys* 55(11), 115502. <https://doi.org/10.7567/JJAP.55.115502>
- Han K, Go D, Tigges T, Rahimi K, Kuehne AJC & Walther A (2017). Social self-sorting of colloidal families in co-assembling microgel systems. *Angew Chem* 129(8), 2208–2214. <https://doi.org/10.1002/ange.201612196>
- Haynes WM, Lide DR & Bruno TJ (2016). *CRC Handbook of Chemistry and Physics*, 97th ed. Boca Raton: CRC Press.
- Hongru A, Xiangqin L, Shuyan S, Ying Z & Tianqing L (2017). Measurement of Wenzel roughness factor by laser scanning confocal microscopy. *RSC Adv* 7(12), 7052–7059. <https://doi.org/10.1039/C6RA26897H>
- Jones CW, Smolinski D, Keogh A, Kirk TB & Zheng MH (2005). Confocal laser scanning microscopy in orthopaedic research. *Prog Histochem Cytochem* 40(1), 1–71. <https://doi.org/10.1016/j.proghi.2005.02.001>
- Konishi N, Torii Y, Kurosaki A, Takatsuka T, Itota T & Yoshiyama M (2003). Confocal laser scanning microscopic analysis of early plaque

- formed on resin composite and human enamel. *J Oral Rehabil* 30(8), 790–795. <https://doi.org/10.1046/j.1365-2842.2003.01129.x>
- Lamprecht A, Schäfer U & Lehr C-M (2000). Structural analysis of microparticles by confocal laser scanning microscopy. *AAPS PharmSciTech* 1(3), 10–19. <https://doi.org/10.1208/pt010317>
- Li C, Zhao Y, He L, Mo R, Gao H, Zhou C, Hong P, Sun S & Zhang G (2018). Mussel-inspired fabrication of porous anodic alumina nanochannels and a graphene oxide interfacial ionic rectification device. *Chem Commun* 54(25), 3122–3125. <https://doi.org/10.1039/C8CC00209F>
- Li L, Li W, Zhang B, Wang B & Zang X (2022a). In-situ observation of growth characteristics of M7C3 carbides in hypoeutectic Fe–Cr–C alloys. *Mater Charact* 191(July), 112143. <https://doi.org/10.1016/j.matchar.2022.112143>
- Li Y, Zou D, Chen W, Zhang Y, Zhang W & Xu F (2022b). Effect of cooling rate on solidification and segregation characteristics of 904L super austenitic stainless steel. *Met Mater Int* 28(8), 1907–1918. <https://doi.org/10.1007/s12540-021-01091-7>
- Lin S, Chen Z, Liu S, Yang Y, Feng X, Ba Y, Yang M & Yang C (2012). Three-dimensional observation of defects in nitrogen-doped 6H-SiC crystals using a laser scanning confocal microscope. *J Mater Sci* 47(7), 3429–3434. <https://doi.org/10.1007/s10853-011-6190-4>
- Malaquias JC, Regesch D, Dale PJ & Steichen M (2014). Tuning the gallium content of metal precursors for Cu(In, Ga)Se<sub>2</sub> thin film solar cells by electrodeposition from a deep eutectic solvent. *Phys Chem Chem Phys* 16(6), 2561. <https://doi.org/10.1039/c3cp54509a>
- Marcellini M, Noirjean C, Dedovets D, Maria J & Deville S (2016). Time-lapse, in situ imaging of ice crystal growth using confocal microscopy. *ACS Omega* 1(5), 1019–1026. <https://doi.org/10.1021/acsomega.6b00217>
- Merson ED, Danilov VA, Linderov ML, Myagkikh PN, Merson DL & Vinogradov A (2018). Assessing fracture surface ductility by confocal laser scanning microscopy. *Procedia Struct Integr* 13, 2152–2157. <https://doi.org/10.1016/j.prostr.2018.12.149>
- Moitzheim S, Put B & Vereecken PM (2019). Advances in 3D thin-film Li-ion batteries. *Adv Mater Interfaces* 6(15), 1900805. <https://doi.org/10.1002/admi.201900805>
- Nakamura M, Yamaguchi K, Kimoto Y, Yasaki Y, Kato T & Sugimoto H (2019). Cd-free Cu(In, Ga)(Se, S)<sub>2</sub> thin-film solar cell with record efficiency of 23.35%. *IEEE J Photovolt* 9(6), 1863–1867. <https://doi.org/10.1109/JPHOTOV.2019.2937218>
- Nakamura S, Tanaka S, Kato Z & Uematsu K (2009). Strength-processing defects relationship based on micrographic analysis and fracture mechanics in alumina ceramics. *J Am Ceram Soc* 92(3), 688–693. <https://doi.org/10.1111/j.1551-2916.2008.02904.x>
- Nishiyabu R & Shimizu A (2016). Boronic acid as an efficient anchor group for surface modification of solid polyvinyl alcohol. *Chem Commun (Camb)* 52(63), 9765–9768. <https://doi.org/10.1039/C6CC02782B>
- Pan L, Liu Y, Yao L, Dan Ren, Sivula K, Grätzel M & Hagfeldt A (2020). Cu<sub>2</sub>O photocathodes with band-tail states assisted hole transport for standalone solar water splitting. *Nat Commun* 11(1), 318. <https://doi.org/10.1038/s41467-019-13987-5>
- Park JS, Dong Z, Kim S & Perepezko JH (2000). CuInSe<sub>2</sub> phase formation during Cu<sub>2</sub>Se/In<sub>2</sub>Se<sub>3</sub> interdiffusion reaction. *J Appl Phys* 87(8), 3683–3690. <https://doi.org/10.1063/1.372400>
- Poeira RG, Pérez-Rodríguez A, Prot AJCM, Alves M, Dale PJ & Sadewasser S (2023). Direct fabrication of arrays of Cu(In, Ga)Se<sub>2</sub> micro solar cells by sputtering for micro-concentrator photovoltaics. *Mater Des* 225, 111597. <https://doi.org/10.1016/j.matdes.2023.111597>
- Pyo S, Lee J, Kim W, Jo E & Kim J (2019). Multi-layered, hierarchical fabric-based tactile sensors with high sensitivity and linearity in ultrawide pressure range. *Adv Funct Mater* 29(35), 1902484. <https://doi.org/10.1002/adfm.201902484>
- Sadewasser S, Salomé PMP & Rodriguez-Alvarez H (2017). Materials efficient deposition and heat management of CuInSe<sub>2</sub> micro-concentrator solar cells. *Sol Energy Mater Sol Cells* 159, 496–502. <https://doi.org/10.1016/j.solmat.2016.09.041>
- Schmid T, Schafer N & Abou-Ras D (2016). Raman microspectroscopy provides access to compositional and microstructural details of polycrystalline materials. *Spectrosc Eur* 28(5), 16–20.
- Shiah Y-S, Sim K, Shi Y, Abe K, Ueda S, Sasase M, Kim J & Hosono H (2021). Mobility–stability trade-off in oxide thin-film transistors. *Nat Electron* 4(11), 800–807. <https://doi.org/10.1038/s41928-021-00671-0>
- Siebert S, Gütay L, Regesch D, Aida Y & Deprédurand V (2013). Why do we make Cu(In, Ga)Se<sub>2</sub> solar cells non-stoichiometric? *Sol Energy Mater Sol Cells* 119, 18–25. <https://doi.org/10.1016/j.solmat.2013.04.014>
- Siopa D, El Hajraoui K, Tombolato S, Babbe F, Lomuscio A, Wolter MH, Anacleto P, Abderrafi K, Deepak FL, Sadewasser S & Dale PJ (2020). Micro-sized thin-film solar cells via area-selective electrochemical deposition for concentrator photovoltaics application. *Sci Rep* 10(1), 14763. <https://doi.org/10.1038/s41598-020-71717-0>
- Sood M, Elanzeery H, Adeleye D, Lomuscio A, Werner F, Ehre F, Melchiorre M & Siebert S (2020). Absorber composition: A critical parameter for the effectiveness of heat treatments in chalcopyrite solar cells. *Progr Photovolt Res Appl* 28(10), 1063–1076. <https://doi.org/10.1002/pip.3314>
- Stanbery BJ (2002). Copper indium selenides and related materials for photovoltaic devices. *Crit Rev Solid State Mater Sci* 27(2), 73–117. <https://doi.org/10.1080/20014091104215>
- Teng X, Li F & Lu C (2020). Visualization of materials using the confocal laser scanning microscopy technique. *Chem Soc Rev* 49(8), 2408–2425. <https://doi.org/10.1039/c8cs00061a>
- Tian R, Li K, Shi W, Ding C & Lu C (2019). In situ visualization of hydrophilic spatial heterogeneity inside microfluidic chips by fluorescence microscopy. *Lab Chip* 19(6), 934–940. <https://doi.org/10.1039/C8LC01336E>
- Vladar A & Postek M (2005). Electron beam-induced sample contamination in the SEM. *Microsc Microanal* 11(S02), 764–765. <https://doi.org/10.1017/S1431927605507785>
- Wan X, Xu J, Xie X-M & Guo B-H (2011). Revealing formation process of microcapsules during in situ polymerization via confocal laser scanning fluorescence microscopy. *Colloid Polym Sci* 289(15–16), 1719–1728. <https://doi.org/10.1007/s00396-011-2494-9>
- Webb RH (1996). Confocal optical microscopy. *Reports on Progress in Physics* 59, 427–471. <https://doi.org/10.1088/0034-4885/59/3/003>
- Witte W, Kniese R, Eicke A & Powalla M (2006). Influence of the Ga content on the Mo/Cu(In, Ga)Se<sub>2</sub> interface formation. In 2006 IEEE 4th World Conference on Photovoltaic Energy Conference, vol. 1, pp. 553–556. Waikoloa, HI: IEEE. May 07–12, 2006.
- Witte W, Kniese R & Powalla M (2008). Raman investigations of Cu(In, Ga)Se<sub>2</sub> thin films with various copper contents. *Thin Solid Films* 517(2), 867–869. <https://doi.org/10.1016/j.tsf.2008.07.011>
- Yasuhara S, Yasui S, Teranishi T, Chajima K, Yoshikawa Y, Majima Y, Taniyama T & Itoh M (2019). Enhancement of ultrahigh rate chargeability by interfacial nanodot BaTiO<sub>3</sub> treatment on LiCoO<sub>2</sub> cathode thin film batteries. *Nano Lett* 19(3), 1688–1694. <https://doi.org/10.1021/acs.nanolett.8b04690>
- Ye S, Shi W, Liu Y, Li D, Yin H, Chi H, Luo Y, Ta N, Fan F, Wang X & Li C (2021). Unassisted photoelectrochemical cell with multimedia modulation for solar water splitting exceeding 4% solar-to-hydrogen efficiency. *J Am Chem Soc* 143(32), 12499–12508. <https://doi.org/10.1021/jacs.1c00802>
- Yio MHN, Mac MJ, Wong HS & Buenfeld NR (2015). 3D imaging of cement-based materials at submicron resolution by combining laser scanning confocal microscopy with serial sectioning. *J Microsc* 258(2), 151–169. <https://doi.org/10.1111/jmi.12228>
- Yoon J, Lee W & Thomas EL (2006). Highly oriented thin-film microdomain patterns of ultrahigh molecular weight block copolymers via directional solidification of a solvent. *Adv Mater* 18(20), 2691–2694. <https://doi.org/10.1002/adma.200600741>
- Zhang SB, Wei S-H, Zunger A & Katayama-Yoshida H (1998). Defect physics of the CuInSe<sub>2</sub> chalcopyrite semiconductor. *Phys Rev B, Condens Matter* 57(16), 9642–9656. <https://doi.org/10.1103/PhysRevB.57.9642>



# TESCAN TENSOR

Integrated, Precession-Assisted,  
Analytical 4D-STEM



Visit us and learn more  
about our TESCAN TENSOR

[info.tescan.com/stem](http://info.tescan.com/stem)